RESEARCH ARTICLE

The role of magma ascent rates and viscosity in explosive and dome eruptions (Kelud volcano, Indonesia)

Sri Budhi Utami[1,2] · Fidel Costa[1,3,4] · Hanik Humaida[5]

Abstract

Magma ascent rate can control the hazard potential of an eruption, but it is difficult to directly determine. Here we investigate the variations in timescales and rates of magma ascent for the three most recent explosive and effusive eruptions of Kelud volcano in Indonesia (1990, 2007, and 2014) using the zoning of volatile elements (OH, Cl, F) in apatite. We found that crystals from the 2007 dome show chemical gradients and increasing concentrations (reverse zoning) in chlorine and/or fluorine towards the crystals' rims whereas those of the 1990 and 2014 explosive eruptions are unzoned. Diffusion modelling of the volatile elements in zoned apatite of the 2007 dome rocks give magma ascent times of up to 3 months, although 65% of them are ≤ 60 days. In contrast, the maximum magma ascent timescales inferred from apatite of the 1990 and 2014 explosive eruptions are 7–8 h. Using the pre-eruptive magma storage depths obtained from petrological and phase equilibria studies, we calculate ascent rates $> 0.4 \times 10^{-3}$ m s^{-1} for the 2007 dome, and $> 3.0 \times 10^{-1}$ m s^{-1} for the 1990 and 2014 eruptions. We also calculated the magma viscosities for each eruption (1990: $10^{3.8-9.3}$ Pa s; 2007: $10^{6.4-13.3}$ Pa s; 2014: $10^{3.6-8.7}$ Pa s), which when combined with the magma ascent rates and magma mass discharge rates correspond well with the expected eruptive styles. Our study illustrates the robustness of modelling apatite zoning in volatile elements to constrain timescales and magma ascent dynamics, and highlights the important role of magma ascent on eruptive styles.

Keywords Kelud · Kelut · Magma ascent rates · Timescales · Viscosity · Apatite

Introduction

The eruptive styles of active volcanoes are difficult to anticipate, but they are key for proper hazards assessment and crises response of impending eruptions. Eruptions can transition from effusive to explosive and vice versa between eruptions for example at Merapi (Costa et al. 2013; Preece et al. 2014), or within one eruptive period such as at Rabaul (Bernard et al. 2022), Redoubt (Bull and Buurman 2013), and more recently at Soufriere St. Vincent (Joseph et al., 2022). Such transitions in eruption style depend on several parameters, including melt volatile contents, melt compositions, magma rheology, and/or magma ascent rates, and these can rapidly change during transport in the conduit and ultimately determine whether magma "flows or blows" (Dingwell 1996; Rutherford 2008; Cassidy et al. 2018). Among the parameters that affect magma explosivity, magma ascent rates appear to exert critical control (Cassidy et al. 2018), but they are generally difficult to determine. Using geophysical data, the timing, and the location

---

Editorial responsibility: H. R. Dietterich

✉ Sri Budhi Utami
  sri.budhi.utami@gmail.com

1   Asian School of the Environment, Nanyang Technological University, 50 Nanyang Avenue, N2-01B-27, Singapore 639798, Singapore

2   Present Address: Département de Géologie, Bâtiment B20, Quartier Agora, Allée du Six Août 12, 4000 Liège 1, Belgium

3   Earth Observatory of Singapore, 50 Nanyang Avenue, Singapore N2-01A-15639798, Singapore

4   Université de Paris Cité, Institut de Physique du Globe de Paris, CNRS, 75005 Paris, France

5   Balai Penyelidikan Dan Perkembangan Teknologi Kebencanaan Geologi, Jalan Cendana, 15, D.I. Yogyakarta, Indonesia

of seismicity that corresponds to the run-up to eruption have been used to obtain constraints on magma ascent rates (e.g. Passarelli and Brodsky 2012; Rasmussen et al. 2018; Roman and Cashman 2018), but most estimates are from experimental and petrological studies. These include quantitative analysis of crystal size distribution and microlites density (Couch et al. 2003; Rutherford 2003; Toramaru et al. 2008) and melt decompression experiments (Martel and Schmidt 2003). In addition, chemical zoning of volatile elements in minerals or melt embayments can be modelled using diffusion laws, from which timescales and magma ascent rates can be obtained (e.g. Myers et al. 2019; Li et al. 2020; Georgeais et al. 2021). Combination of micro-textures and geochemistry of the crystal cargo can yield timescales that are comparable to some volcano monitoring techniques (e.g. seismicitySaunders et al. 2012; Kilgour et al. 2014; Albert et al. 2015). These timescales of magma ascent can then be converted to ascent rates assuming magma storage depths are also known. Such depths below the volcano can be obtained from phase equilibria experiments (e.g. Andújar et al. 2013; Cadoux et al. 2014; Utami et al. 2022), or from mineral-melt geobarometry (Blundy and Cashman 2008; Putirka 2008). Alternatively, geophysical studies employing tomography can be used to calculate storage depth of many volcanoes (Puspito and Shimazaki 1995; Widiyantoro and van der Hilst 1996; Widiyantoro et al. 2018), although the uncertainty of magma storage depths of some of these studies yield larger ranges of potential magma ascent rates.

Among the various petrological tools available to constrain volatile budgets and magma ascent rates, apatite is an increasingly popular mineral (e.g. Stock et al. 2016; Humphreys et al. 2021; Bernard et al. 2022), as it can incorporate several volatile elements in its crystal structure $[Ca_5(PO_4)_3(Cl, F, OH)]$. Apatite has been used to investigate a range of processes, including the pre-eruptive melt volatile concentrations (Scott et al. 2015); estimate volatile budgets and ascent rates (Li et al. 2021; Bernard et al. 2022); and reveal the relationship between volatile dynamics and an eruption's explosivity (Stock et al. 2016); the record of metasomatism and fluid movement in the crust (Harlov 2015); track arc magma evolution (Nathwani et al. 2020); record carbonate assimilation into magma (Wang et al. 2014), or to investigate estimate lunar water contents (Boyce et al. 2014).

Here we use apatite to constrain magma ascent rates from three historical eruptions at Kelud (Kelut) volcano in East Java, Indonesia. Kelud has produced some of the most hazardous historical eruptions in Southeast Asia (Goode et al. 2018; Maeno et al. 2019; Utami et al. 2022). Hazards from explosive eruptions of Kelud are capable of wreaking havoc across the island of Java. For example, the 2014 eruption produced voluminous ash and ejecta that severely impacted several cities. Hazards included building collapse from tephra accumulation, destructive lahars, extensive building damage, and ash inhalation (Blake et al. 2015; Williams et al. 2020). On the other hand, dome emplacements such as in 2007 were less immediately hazardous but may have enabled accumulation of excess volatiles underneath the dome, and thus increase the explosivity potential of the next eruption (Utami et al. 2022). In this study we characterized the volatile chemistry of apatite crystals from the 1990, 2007, and 2014 explosive and effusive eruptions of Kelud. We also modelled the zoning of Cl, F, and OH in apatite crystals to obtain timescales of magma ascent and degassing. From this parameter we calculated magma ascent rates that, combined with magma viscosities, are used to infer the possible magmatic processes associated with each eruptive style.

Kelud volcano and its historical eruptions

Kelud (Kelut) is an active volcano in East Java, Indonesia classed as a basaltic andesite semi-plugged strato-cone (Whelley et al. 2015) that has produced > 30 explosive eruptions and effusive dome extrusions since 1000 CE, with a mean recurrence interval of ~ 23 years (e.g. Global Volcanism Program 2013; Kusumadinata and van Padang 1979; van Padang 1983). The volcano is monitored with a dedicated observatory (Global Volcanism Program 2013) by the Centre of Volcanology and Geological Hazards Mitigation of Indonesia (CVGHM, or PVMBG in Bahasa Indonesia). The explosive eruptions in 1990 and 2014 were short-lived, with unrest signals escalating within hours from the onset of unrest to eruption, making them challenging to forecast (Nakamichi et al. 2017). In contrast, the 2007 dome extruded effusively after a month of unrest, which included elevated seismicity and carbon dioxide emissions into the lake (Hidayati et al. 2009; Caudron et al. 2012). Unrest signals for all three eruptions consisted of heightened seismicity, deformation, and changes of the lake temperature above background levels (Lesage and Surono 1995; Vandemeulebrouck et al. 2000; Hidayati et al. 2019) (see Table S1). Both the 1990 and 2014 explosive events were preceded with an almost exponential increase in seismicity around 12 h before each eruption (Lesage and Surono 1995; Hidayati et al. 2019), but this trend was not observed before the 2007 dome. Several short-lived unrest episodes or crises occurred after the 1990 eruption and until the 2014 eruptions (Global Volcanism Program 1991) including 1996 and 2001, but they did not result in an eruption (Global Volcanism Program 1996; 2001).

Previous studies on timescales of magmatic processes at Kelud used the Mg-Fe interdiffusion in reversely zoned pyroxenes before the 1990 eruption (Utami et al. 2021), which they compared with timings of seismic and hydroacoustic unrest and run-up times (Lesage and Surono 1995; Vandemeulebrouck et al. 2000). Timescales of Mg-Fe

interdiffusion in pyroxenes span weeks to months, and were attributed to degassing and fluid accumulation. These timescales also overlapped with the onset of seismic and hydro-acoustic unrest that began around three months before the eruption. The exponential run-up in seismicity that began ~ 12 h before the onset of the 1990 eruption gave magma ascent rates of ~ 0.2 m s^{-1} based on magma storage depths of 6–7 km (Lesage and Surono 1995; Utami et al. 2021, 2022). Other estimates of magma ascent rates for the more recent 2014 eruption are around 4–5 m s^{-1} (Cassidy et al. 2019), which were calculated using shallower storage depths of 2–3 km.

Methodology

We studied apatite crystals from one main-stage and one late-stage pumices of the 1990 deposits, one fragment from the 2007 lava dome, and two pumices from the sub-Plinian phase of the 2014 eruption. These are the same samples as in Utami et al. (2021) and Humaida (2013), where more details about sample locations and descriptions can be found.

Chemical Analyses of Apatite

We obtained backscattered electron (BSE) images of carbon-coated thin sections for each sample, and identified apatite based on their Electron Dispersive Spectra (EDS) using a JEOL-JSM 7800F scanning electron microscope (SEM) at the Earth Observatory of Singapore (EOS). We then mapped the apatite grains for Mg, Fe, Cl, F, and S in Wavelength Dispersive Spectra (WDS) mode on the JEOL JXA-8530F field emission electron microprobe (EPMA) at the Facility for Analysis Characterisation Testing and Simulation (FACTS-NTU), Nanyang Technological University, Singapore (NTU). Guided by these elemental maps, we selected target crystals for EPMA analyses.

Target apatite crystals were analyzed in spot mode broadly following the methodology outlined in Li et al. (2021), using a 15 kV beam and 10 nA current, but with 1–4 μm beam size. On peak counting times are 550 s (F – 60 s; Na – 10 s; Mg – 100; Fe – 40 s; Mn – 40 s; Ce – 60 s; Ca – 20 s; Cl – 60 s; P – 20 s; Si – 60 s; S – 80 s). Profiles of zoned apatite crystals from the 1990, 2007, and 2014 eruptions were analyzed using a 10 nA current and 1–4 μm beam size. The structural formula of each apatite was calculated using approach #1 of Ketcham (2015), which was adapted based on an estimate of the [OH] content. We used a threshold of < 5% deviation from the ideal cation ratio of 5/3 to discard non-stoichiometric apatite analyses and/or mixtures. The mole fraction of volatile elements in the M2 column anion sites are given as X_{Cl}, X_F, and X_{OH}, respectively. The

OH anion was calculated by subtracting the atom per unit formula of Cl and F from the site total and normalizing the value according to:

$$X_{OH} = {}^1\!/_2 \times [2 - (Cl + F)] \tag{1}$$

Here we refer to the calculated OH as OHc. Relative errors from the EPMA analyses are 1–3% for X_{Cl}, 1–4% for X_F, and the propagated errors are 1–33% for the calculated X_{OH}. Some of the compositional profiles in the 1990 apatite crystals had major element oxide totals that were < 98 wt. %, perhaps due to thicker carbon coating (> 15 nm) present in some thin sections. We determined the orientation of the crystallographic axes of apatite (α and γ for a and c-axes, respectively) using the Electron Back-Scatter Diffraction (EBSD) mode in the SEM at EOS. These crystallographic orientations were used to calculate the angle between each EPMA profile and the crystallographic axes needed for diffusion coefficient correction (Costa et al. 2008), with an EBSD conversion code employing MTEX Texture Analyses Toolbox. The EBSD conversion code for apatite and other minerals can be obtained with the following link: https://github.com/jago2216/EBSD-Codes.

Modelling timescales and ascent rates from apatite

The Cl-F-OH diffusion in apatite was modelled as a multicomponent system and involves interaction between volatile species (Li et al. 2020), and we used a MATLAB code associated with the online ApTimer application that models multi-component Cl-F-OH diffusion in apatite (Li et al. 2020) (See Supplementary Material). The model also used a finite difference solution of the diffusion equation in one dimension, as it was appropriate given the length of the profiles and size of the crystals we investigated. Due to the large anisotropy of diffusion for many elements in apatite, we used the acute angles between the profiles and the crystallographic a- and c-axes (α and γ, respectively) to correct for Cl, F, and OH diffusion coefficients from Li et al. (2020). The anisotropy is such that the diffusion parallel to the c-axis is considerably faster than parallel to the a-axes (Li et al. 2020). Thus a correction factor was applied to the diffusion coefficients (D_i) of three profiles that were parallel to the a-axes:

$$D_{Cl||a} = 166 \times D_{Cl||c}, \text{ where } D_{Cl||a} = D_{Cl||b} \tag{2}$$

$$D_{F||a} = 19 \times D_{F||c}, \text{ where } D_{F||a} = D_{F||b} \tag{3}$$

$$D_{OH||a} = 46 \times D_{OH||c}, \text{ where } D_{OH||a} = D_{OH||b} \tag{4}$$

These factors were determined by first calculating the diffusion coefficients at 950 °C for Cl, F, and OH parallel

to the *c*-axis, and then dividing their values by diffusion coefficients parallel to the *a*-axis at the same temperature. This was necessary because Li et al. (2020) only determined the diffusion coefficients of these volatile elements parallel to *a*-axis at 950 °C. For further information, readers are encouraged to consult Li et al. (2020). Here we assume that the activation energy for these elements does not change with crystallographic orientation, which is the case for some minerals and elements (e.g. Fe–Mg in olivine; Dohmen and Chakraborty 2002). We mostly used the Cl profile to obtain best fit timescales as it was the most prominently zoned and precisely measured element, but in a few cases, we used the F profile instead. The initial boundary conditions were chosen by visual inspection of the 1-D profile shape and used to determine the most suitable core and rim compositions. A constant rim composition was used, and diffusion towards the core generated the observed concentration gradients (Li et al. 2020). This is a simplification of the diffusion process, as the composition of the apatite crystal rim likely changed in a complex manner during magma ascent due to loss of volatiles and microlite crystallization. Using compositions that change with time at the boundary would give comparatively shorter times (Costa et al. 2008). We used temperatures of 974–980 ± 39 °C for the three eruptions, as constrained through geothermobarometry and phase equilibria results reported in Utami et al. (2022). All inputs into the ApTimer application are listed in Table 1.

For unzoned apatite from the 1990 and 2014 eruptions, we obtained the maximum time of diffusion using the Cl concentration on the condition that if there was a given diffusion length (see below), we would have been able to detect it in our elemental Cl maps and EPMA profiles. We thus neglected the multicomponent diffusion formulation and used a simplified diffusion equation for the penetration depth from the crystal rim towards the interior to calculate time (Costa et al. 2008):

$$x = \sqrt{4D_{Cl}t} \tag{5}$$

where *x* is the diffusion distance, which we chose to be 4 μm. D_{Cl} is the diffusion coefficient for Cl from Li et al. (2020); no correction factor necessary as several grains we investigated had profiles that were parallel to the *c*-axis. Magma ascent rates were calculated using the timescales and magma storage depths of 7 km, or storage pressures of 175 MPa derived from phase equilibria experiments and geothermobarometry (Utami et al. 2021, 2022), along with a mean crustal density of 2640 kg m^{-2} (Jeffery et al. 2013).

Magma viscosity calculations

To quantitatively compare the magma physical properties between the different eruptions, we first calculated the melt viscosity using the formulation of Giordano et al. (2008). For this, we used the calculated matrix glass composition calculated from Utami et al. (2022) for a range of pre-eruptive temperatures (average T = 980 ± 39 °C) and the same pre-eruptive water content in the melt as our starting point (4 wt. %), which was chosen based on previous studies on the same samples (Utami et al. 2021, 2022). To incorporate the effect of crystals, we calculated the effective viscosity for all three eruptions using the Einstein-Roscoe equation (e.gEinstein 1906; Roscoe 1952; Gonnermann and Manga 2013):

$$\eta_{eff} = \eta_{melt} \times \left(1 - \frac{\phi}{\omega}\right)^{-2.5} \tag{6}$$

where η_{eff} is the effective viscosity, η_{melt} is the melt viscosity, $\varnothing$ is the volume fraction of crystals, and ω is the threshold volume fraction of crystals required for to transition to a rigid system, for which we used the value of 60 vol.%. The phenocryst content of the 1990 and 2014 eruption deposits range from 28 to 47 vol. % (Utami et al. 2022), which allowed us to use the Einstein-Roscoe equation. The phenocryst content of the 2007 dome are up to 70 vol. %, which precludes accurate estimation of the effective viscosity for the dome rocks with Eq. 6. We thus compared several viscosity models capable of calculating effective viscosities for up to 80 vol. % (Caricchi et al. 2007; Costa et al. 2009) and followed a conceptually accurate model (Faroughi and Huber 2015; Moitra and Gonnermann 2015; Moitra et al. 2018), which is explained in greater detail below.

Some viscosity models such as the Moitra and Gonnermann (2015), required detailed information on crystal shape parameters, packing fraction and aspect ratios for both microlites and phenocrysts. However, we made a simplification by concentrating on crystal size and shape parameters of phenocrysts. The mineral assemblages of all samples are dominated by prismatic plagioclase crystals, with some prismatic pyroxene and crystal clots, as previously documented in Utami et al. (2021, 2022). The relatively high crystal content of the 1990 (31–47 vol. %) and 2007 (67–71 vol. %) eeruptions made the maximum packing fraction (φm) the most important factor. The aspect ratios of phenocrysts and crystal clots were determined with Feret's diameter of BSE images using ImageJ (Schneider et al. 2012) for the 2007 dome (n = 80), the 1990 (n = 100) and 2014 (n = 78) eruptions. Based on this results, we used parameters corresponding to a suspension of large spheres (S) for the 1990 and 2014 eruptions, and a mixture of large and small spheres (Ss) for the 2007 dome. The parameters we used are reported in Table 3 and n$_{min}$ was estimated from Fig. 10 of Moitra and Gonnermann (2015). To be able to compare the effective viscosities of all three eruptions, we also calculated the effective viscosities for the 1990 and 2014 eruptions with the same viscosity models as the 2007 dome.

Table 1 Apatite diffusion coefficients and timescales modelled using ApTimer (Li et al. 2020), along with best fit magma ascent rate (v_{ascent})

Apatite crystal	Traverse ID	texture	Input T (°C)[a]	α (°)	γ (°)	D_{Cl} (×10⁻¹⁷ m² s⁻¹)	D_F (×10⁻¹⁷ m² s⁻¹)	D_{OH} (×10⁻¹⁹ m² s⁻¹)	Maximum hours	Δt(-)	Δt(+)	Minimum v_{ascent}×10⁻¹ (m s⁻¹)
1990 Sub-Plinian eruption												
1	PL1new-px4-apa1-r2r	groundmass	980	90	0	3.9	-	-	7	4	11	3.0
2	PL1new-gm7-apa-trvlong-r2r	groundmass	980	90	0	3.9	-	-	7	4	11	3.0
	2014 Sub-Plinian eruption								Maximum hours	Δt(-)	Δt(+)	Minimum v_{ascent}×10⁻¹ (m s⁻¹)
1	14PUM1-1-amph-gm-apa1_trv2-r2c	groundmass	980	90	0	3.9	-	-	7	4	11	3.0
2	14PUM2-1-gm1-apa1-tv1short-r2r-4um	groundmass	980	90	0	3.9	-	-	7	4	11	3.0
3	14PUM2-1-gm3-apa1-r2c	groundmass	980	90	0	3.9	-	-	7	4	11	3.0
4	14PUM1-1-amph6-apa1_trv2-r2c	amphibole pseudomorph inclusion	980	90	0	3.9	-	-	7	4	11	3.0
	2007 dome extrusion								best fit t (days)	Δt(-)	Δt(+)	range of v_{ascent}×10⁻³ (m s⁻¹)
1	07B-glom3-apa1-long	groundmass	980	81	167	3.8	7.2	6.6	21	8	4	3.1–6.3
	07B-glom3-apa1-short	groundmass	980	174	92	0.1	0.8	0.3	158	17	17	0.4–0.6
2	07B-gm1-apa1-long	groundmass	980	93	23	3.3	6.4	5.8	6	1	1	10–16
	07B-gm1-apa1-short	groundmass	980	173	95	0.1	0.8	0.3	83	8	8	0.9–1.0
3	07B-gm2-apa1-long-r2c	groundmass	980	92	3	3.9	7.5	6.9	25	6	4	2.7–4.2
	07B-gm2-apa1-short-r2c	groundmass	980	111	108	0.4	0.9	0.7	63	21	88	0.5–1.9
4	07B-gm3-apa1-long-r2c	groundmass	980	94	17	3.6	6.9	6.3	9	2	3	6.7–10.4
	07B-gm3-apa1-short-r2c	groundmass	980	48	43	2.1	4.4	3.9	15	3	2	4.7–6.5
5	07B-gm4-apa1-short-r2c	groundmass	980	138	48	1.8	3.8	3.3	75	13	29	1.3–0.8
6	07B-px6-apa1-r2r	groundmass	980	100	17	3.6	7.0	6.4	17	2	2	4.2–5.2
7	07B-gm5-apa1-long-r2c	groundmass	980	100	115	0.7	1.3	1.2	58	13	67	0.6–1.7
8	07B-px9new-gmox-apa-short-r2c	groundmass	980	90	0	3.9	7.6	6.9	2	1	1	24–52
	07B-px9new-gmox-apa-short-r2c	groundmass	980	0	90	0.0	0.8	0.3	67	10	42	0.7–1.4

Table 1 (continued)

Apatite crystal	Traverse ID	texture	Input T (°C)[a]	α (°)	γ (°)	D_{Cl} ($\times10^{-17}$ m² s⁻¹)	D_F ($\times10^{-17}$ m² s⁻¹)	D_{OH} ($\times10^{-19}$ m² s⁻¹)	Model timescales		Magma ascent rate[b]	
9	07B-pseudo1-apa1-r2c	amphibole pseudomorph inclusion	980	61	55	1.3	2.7	2.3	1.3	0.4	1.3	31–94
10	07B-px5-apa1-r2c	pyroxene hosted inclusion	980	45	117	0.8	1.9	1.5	20	3	5	3.1–4.7
11	07B-px15-incl-apa1-r2c	pyroxene hosted inclusion	980	147	57	1.2	2.8	2.3	30	9	5	2.2–3.8
12	07B-glom1-apa1-long-r2c	pyroxene hosted inclusion	1028	169	98	0.4	2.7	1.8	175	8	8	0.4–0.5

a. Magma ascent rates for 1990 and 2014 are determined using temperatures calculated using temperatures calculated from the Opx-melt geothermometer (SEE= ± 39 °C), from Utami et al. (2022)

b. Magma ascent rates are calculated using a depth of 7 km, based on storage depths of 175 ± 25 MPa (Utami et al. 2022)

The α and γ are angles of traverses relative to the a- and c-axis respectively

For apatite crystal 'px9new-gmox', the angles relative to a- and c-axes were not measured, so we calculated two end-member ascent rates parallel to either axes

These viscosity models also require the ascent rate and conduit diameter, which are a priori unknown. However, the mass discharge rate (MDR) for the three eruptions were calculated by Maeno et al. (2019), and these can be related to the exit velocity (v_e) in m s⁻¹, magma density at discharge ($\rho_{discharge}$) in kg m⁻³, and conduit cross-sectional area ($A_{conduit}$) in m² through the following equation (See Table 2 for a summary of calculated parameters):

$$MDR = \rho_{discharge} \times v_e \times A_{conduit} \tag{7}$$

The magma exit velocity is in principle different and higher than the magma ascent velocity we have calculated from the apatite diffusion models, and the magma density at pre-eruptive conditions is also different and higher than that at exit, when magma can be full of gas bubbles due to volatile exsolution. However, for the 2007 dome eruption the magma ascent velocity and the density we calculate at depth are very similar to the values at exit, and we have used them to obtain a range of conduit diameters and thus calculated the viscosity of the 2007 magma. For the 1990 and 2014 eruptions we used the Einstein-Roscoe equation to calculate their respective viscosities. Moreover, we also used the MDR values and measured density (1400 kgm⁻³) for the 1990 and 2014 eruptions reported by Maeno et al (2019), which we report in Table 3 and Fig. 6. These values, together with the ascent rates from the apatite, were used to calculate the magma viscosity of the 1990 and 2014 magmas using various viscosity models that would better account for the crystal content and strain rate (Caricchi et al. 2007; Costa et al. 2009; Faroughi and Huber 2015; Moitra and Gonnermann 2015; Moitra et al. 2018). For the 2007 dome, the strain rate was needed for the Caricchi et al. (2007) and the Costa et al. (2009) viscosity models, which we calculated by dividing the magma ascent rate with the conduit radius (Moitra et al. 2018) (Table 3).

Results

Apatite crystals from the 1990 main-stage pumices are found in the groundmass (Fig. 1a), and as inclusions in pyroxenes and partially reacted amphibole phenocrysts (Fig. 1b, 1c). These apatite crystals are typically subhedral with rounded edges to euhedral, with sizes of around 100–500 μm. We find apatite in similar textural positions in the late-stage pumice (Fig. 1d, 1e), except for the apatite found in the quartz-bearing enclaves, which could have previously been groundmass apatite (Fig. 1d, 1f). Some apatite crystals are found in close textural association with magnetite and ilmenite or are found attached to phenocrysts. The apatite of the 2014 eruption apatite has similar textural relations and sizes as that of the 1990 main-stage pumices (Fig. 1j, 1l), but it is also found

Table 2 Estimated pre-eruptive conduit geometry of the 1990, 2007, 2014 eruptions

Eruption Year	1990	2007	2014
Explosive/Effusive	Sub-Plinian	Effusive Dome	Sub-Plinian
DRE volume ($\times 10^6$ m^3)[1]	63	35	212
Mass ($\times 10^9$ kg)[a]	156	88	530
Mean Discharge Rate ($\times 10^4$ kg/s)[a]	510	0.58	5400
Max Discharge Rate ($\times 10^4$ kg/s)[a]	1000	1.9	6500
Magma density at discharge (kg m^{-3})	1400	2514	1400
Minimum v_{ascent} (m s^{-1})[b]	0.27	0.005	0.30
Min. Conduit cross-section area, A ($\times 10^3$ m^2)	13.5	0.5	129
Max. Conduit cross-section area, A ($\times 10^3$ m^2)	26.5	1.5	155
Conduit radius[c](m)	66–92	12–22	202–222
Conduit diameter[c] (m)	131–183	24–43	404–443

a. Dense rock equivalent (DRE) volume, erupted mass, and maximum discharge rates were taken from Maeno et al. (2019)

b. Minimum ascent rate assumed to start from the base of the conduit

c. Minimum conduit radius and diameter was calculated with the mean discharge rate

inside melt inclusions (Fig. 1k). In contrast, apatite crystals in the 2007 dome, particularly in the groundmass, are significantly larger (< 1000 μm) than either of the 1990 and 2014 eruption deposits (Fig. 1g, 1i, 1h). Apatite in the 2007 dome rocks is also subhedral to euhedral and found as inclusions in melt embayments in glomerocrysts (Fig. 1g) or wedged between phenocrysts (Fig. 1h).

Apatite from the 2007 eruption overlap in composition with 1990 and 2014 crystals, but feature texturally distinct populations (Figs. 2 and 3). For example, single 2007 dome apatite crystals mostly overlap with those from the other eruptions in F (1.4–1.7 wt. %) and Cl (0.6–1.0 wt. %) with only two grains recording lower Cl (0.6–0.8 wt. %). The 2007 dome apatite crystals in contact with the melt, such as those found in the groundmass or wedged in between phenocrysts, commonly show reverse apatite zoning with rims are generally slightly higher in Cl than in cores (Fig. 2b). This is confirmed in X-ray elemental maps, where we see that Cl increases from core to rim (Fig. 2c, e). Apatite not in contact with the melt is unzoned (Fig. 2d).

Apatite from the 1990 and 2014 deposits mostly overlap in composition (Fig. 3), with some exceptions. The 1990 main-stage apatite volatile contents largely overlap irrespective of their textural positions (groundmass or inclusions), with 0.9–1.6 wt. % F, and 0.6–0.9 wt. % Cl. Apatite in the late-stage pumice is, however, enriched in F (2.0–2.4 wt. %), and in Cl (1.1–1.3 wt. %) compared to the main-stage apatite (Fig. 3a). This is consistent with previous evidence of the late-stage interstitial melt being more evolved than in the main-stage pumice (Utami et al. 2021). The 2014 apatite volatile compositions overlap with those of the 1990 main-stage apatite in F (1.0–1.7 wt. %) and Cl (0.6–1.7 wt. %). However, there are some chemically distinct populations in the 2014 eruption (Fig. 3b). For example, the amphibole-hosted apatite

crystals have significantly higher Cl concentrations (1.7 wt. %) compared to the rest (0.6–1.0 wt. %).

None of the apatite crystals from the 1990 nor the 2014 pumices are visibly zoned in volatile elements with the range of analytical techniques we have used (Fig. 3b-e). The 2007 dome apatite crystals are different from the 1990 and 2014 eruption in that they are reversely zoned in Cl, F, and OH_c over lengths of about 9–25 μm. Rim compositions of zoned apatite are 0.9–3.2 wt. % F and 0.5–1.6 wt. % Cl, whereas core compositions have 1.4–1.7 wt. % F and 0.6–0.9 wt. % Cl. We identified two main types of zoning in the 2007 apatite crystals (Fig. 4a-d vs Fig. 4e-f). One common feature in the groundmass apatite is reverse zoning in Cl, which increases towards the rims (reverse zoning) (Fig. 2). F and OH_c are mirror images in concentration of those of Cl from core to rim (Fig. 4a-d). Other apatite crystals show a reverse zoning with an increase in F towards the rims (Fig. 4e-h), alongside a slight increase in Cl, whereas OH_c decreases. This zoning is found in crystals that are not exposed to the melt or only partly exposed (e.g. wedged between phenocrysts, melt tubes/re-entrants, or unsealed melt pockets in glomerocrysts). Only the apatite crystals from the 1990 late-stage pumice, and the amphibole-hosted apatite from 2014 display significantly different compositions. In summary, we found that apatite from the 1990 and 2014 eruption are unzoned in volatile elements, whereas apatite from the 2007 dome displayed two types of zoning patterns. The differences in the presence or absence of zoning is likely related to the different modes of magma degassing between the two eruption styles, such that explosive eruptions involve magma ascent rates that are considerably faster than that of domes. In the following sections we interpret these zoning patterns in the context of volcanic processes and historical unrest at Kelud.

Table 3 Input parameters and results of melt and effective viscosity calculations for 1990, 2007, and 2014 eruptions

Year	1990	2007	2014
Volcano Explosivity Index	4	2	4
Eruption Style	Sub-Plinian	Effusive Dome	Sub-Plinian
Crystal content (vol. %)[a]	31–47	68–70	28–32
Initial H_2O content in melt (wt. %)[a]	4–6		
Storage pressure (MPa)[a]	175 ± 25		
T (Opx-melt, Two-pyroxenes) (°C)[a,b]	976 ± 39	980 ± 60	974 ± 39
Length of conduit (m)[c]	6800 ± 1000		
Syn-eruptive H_2O content in melt (wt. %)[d]	0–4		
$\log_{10}$ melt viscosity, η (Pa s)[e]	3.4–6.9	3.8–7.4	3.3–6.8
Minimum v_{ascent} (m s^{-1})	0.3	0.0005	0.3
strain rate, γ` ($\times 10^{-3}$ s^{-1})	4.2	0.04	1.3

Particle shape information, fitting parameters, and relative viscosity

Caricchi et al. (2007), Costa et al. (2009)			
Fitting parameters for Caricchi et al. (2007)			
Equation 6, ϕ mx	0.65	0.58	0.65
Equation 7, δ	2.9	11.4	4.6
Equation 8, γ	8.3	2.8	7.4
Equation 9, α	0.9993	0.9999	0.9994
Fitting parameters for Costa et al. (2009)			
Equation 7, ξ	0.0007	0.0001	0.0006
Relative viscosity by model, $\log_{10} \eta$			
Caricchi et al. (2007)	0.4–0.8	5.4–5.9	0.3–0.4
Costa et al. (2009)	0.5–0.9	5.0–6.7	0.4–0.5
Faroughi & Huber (2015)			
Minimum suspension volume fraction, Φ min	0.31	0.68	0.28
Maximum suspension volume fraction, Φ max	0.47	0.70	0.32
Ratio of suspension packing, Φ[f]	0.84	0.26	0.87
relative viscosity, $\log_{10} \eta$	0.5–1.1	4.2–5.4	0.4–0.5
Moitra et al. (2018, Moitra and Gonnermann 2015)			
Average phenocryst aspect ratio	1.8	1.1	1.7
Type of suspension[g]	Large spheres (S)	Packed large + small spheres (Ss)	Large spheres (S)
Maximum packing fraction, ϕm	0.64	0.80	0.64
Maximum measured packing fraction, ϕmax	0.47	0.82	0.32
Selected fitting parameters[g]			
Fitting parameter for Eq. 13, α	2.16	2.34	2.16
Fitting parameter for Eq. 15, τ^*	0.0034	0.335	0.0034
Flow index at ϕmax, n_{min}	0.5–0.7	0.6–0.7	0.5–0.7
Relative viscosity, $\log_{10} \eta$	1.5–2.5	2.6–3.5	1.1–1.8

Effective magma viscosity, $\log_{10} \eta$ (Pa s)

Einstein-Roscoe (Einstein 1906; Roscoe 1952)	4.2–7.8	N.A.[h]	4.0–7.5
Caricchi et al. (2007)	3.8–7.7	9.2–13.3	3.6–7.2
Costa et al. (2009)	3.9–7.4	8.7–12.4	3.7–7.2
Faroughi & Huber (2015)	3.9–7.5	8.0–11.6	3.7–7.2
Moitra et al. (2018, Moitra and Gonnermann 2015)	5.8–9.3	6.4–11.0	4.5–8.7

Table 3 (continued)

a. The crystal content, water content, temperature, and storage pressure are all taken from Utami et al. (2022)

b. The temperatures were from Utami et al. (2022), using the Opx-Melt and two-pyroxene geothermometers (Putirka 2008)

c. The conduit length was calculated from the storage pressure assuming an average crustal density of 2640 kg m^{-3} (Jeffery et al. 2013)

d. The syn-eruptive water content range was chosen to simulate the viscosity change where the magma initially has 4 wt. % water (Utami et al. 2022)

e. The melt viscosity was calculated using the viscosity model of Giordano et al. (2008) with the calculated matrix composition in Utami et al. (2022)

f. Maximum suspension volume fraction, $\psi M = 0.74$ for closely packed face centred cubic structures (Faroughi and Huber 2015)

g. Suspension types and fitting parameters are taken from Table 3 and 4 from Moitra and Gonnermann (2015), respectively. n_{min} is estimated from Fig. 10 of Moitra and Gonnermann (2015)

h. Minimum crystal fraction exceeds packing $\phi_{max} = 0.6$, and thus range is not included for the 2007 dome

N.A. = not applicable (see footnote h)

Discussion

Interpretation of the volatile zoning patterns in apatite

We propose that the type of zoning of Cl, F, and OH in apatite during magma ascent can be related to the combined effect of magma degassing (e.g. water loss from the melt) during ascent and the associated microlite crystallization (e.g. Blundy and Cashman 2000; Couch et al. 2003; Martel 2012). In the previous sections, we showed that volatile zoning profiles from the 2007 dome apatite population display two types of zoning: one where Cl increases from core to rim, with variable OH, and F (type 1) (Fig. 4a-d); and another where F increases from core to rim, with variable Cl and OH (type 2) (Fig. 4e-f). However, due to the coupled partitioning and uphill diffusion of OH, Cl, and F into the same crystallographic site of apatite (Li et al. 2020), their concentration gradients are not straightforward to interpret. Water loss from the volatile exsolution typically leads to crystallization of microlites of minerals including plagioclase, pyroxenes, and Fe-Ti oxides (e.g. Blundy and Cashman 2000; Toramaru et al. 2008; Bernard and Bouvet de Maisonneuve 2020). Given that these minerals do not incorporate significant amounts of Cl and F, we propose that the concentrations of these volatiles would increase in the melt, which would also increase in apatite such as in type 1 zoning of zoned apatite crystals. The amount of increase may depend on several interrelated factors, including the value of the partitioning coefficient of volatile elements between apatite and the surrounding melt, and their dependence on intensive melt parameters such as temperature (Li and Costa 2019). The relationship could also change if there is pressure- and temperature-dependent partitioning of these elements between the melt and apatite in the presence of an exsolved fluid phase or brine (Li et al. 2021). Despite this range of possible scenarios, we hypothesize that the volatile zoning in Kelud apatite is likely driven by coupled magmatic-volatile processes, including degassing, microlite crystallization, and in the case of the 2007 zoned dome apatite (which records slower timescales

than 1990/2014), diffusion from slow ascent coupled with degassing (Utami et al. 2021). This lack of zoning likely reflects fast magma ascent, and thus limited transport time available to develop measurable chemical zoning.

Apatite crystals with F reverse zoning (type 2) are found as inclusion in other minerals, or only partly open to the melt may behave similarly to volatile trends in melt inclusion embayments (e.g. Myers et al. 2019, 2021; Saalfeld et al. 2022). In this case, the apatite volatile zoning may not be fully controlled by degassing-induced crystallization. Rather, the zoning could reflect a localized temperature decrease, as F partitioning between apatite and melt is more sensitive towards temperature dependence than both Cl and OH (Li and Costa 2019).

Other studies of zoned apatite have shed light on the role of volatile on pre-eruptive processes. For example, Li et al. (2021) compared the volatile budget of zoned apatite from the 2006 versus unzoned apatite from 2010 rocks of Merapi volcano, and proposed that input of deep volatile into shallow magma column before the 2010 eruption led to fast magma ascent rates, and thus higher degree of explosivity. At other magmatic systems including Campi Flegrei and Laacher See, volatile zoning in apatite are interpreted to reflect the progressive volatile saturation in the system as a result of fractional crystallization, and re-organization of the magmatic system (Stock et al. 2018; Humphreys et al. 2021). Even so, few studies use apatite as a tool to explore magmatic timescales and ascent rates. For example, differences in magma ascent dynamics have been observed in stratovolcanoes such as Merapi (Li et al. 2021), and caldera eruptions, such as Rabaul caldera (Bernard et al. 2022). Our case study thus complements existing literature on apatite as an important tool in volcano petrology.

Apatite timescales and their relation to volcanic unrest

The 2007 Dome eruption.

A total of 17 diffusion timescales (with typical diffusion lengths of 10–30 μm) were obtained from 12 different

Fig. 1 BSE/SEI images of apatite crystals in various textural environments in the 1990, 2007, and 2014 rocks. Abbreviations are as follows: Ap = apatite; Gm = groundmass; Amph = amphibole (pseudo = pseudomorph); Cpx = clinopyroxene; Opx = orthopyroxene; Mag = magnetite; Ilm = ilmenite; MI = melt inclusion. In 1990 main- and late-stage pumices, apatite is found in: (a) the groundmass; (b) as Amph-hosted inclusion; (c) Cpx-hosted inclusion; (d) Opx-hosted inclusion; (e) inclusions in Amph pseudomorphs; (f) as inclusions in quartz-bearing enclaves; (g) glomerocrysts; (h) embedded between phenocrysts; (i) groundmass phase; (j) Cpx-hosted inclusions; (k) melt inclusion daughter phase; and (l) Amph-hosted inclusions. White scale bars are 10 µm, whereas red scale bars are 100 µm
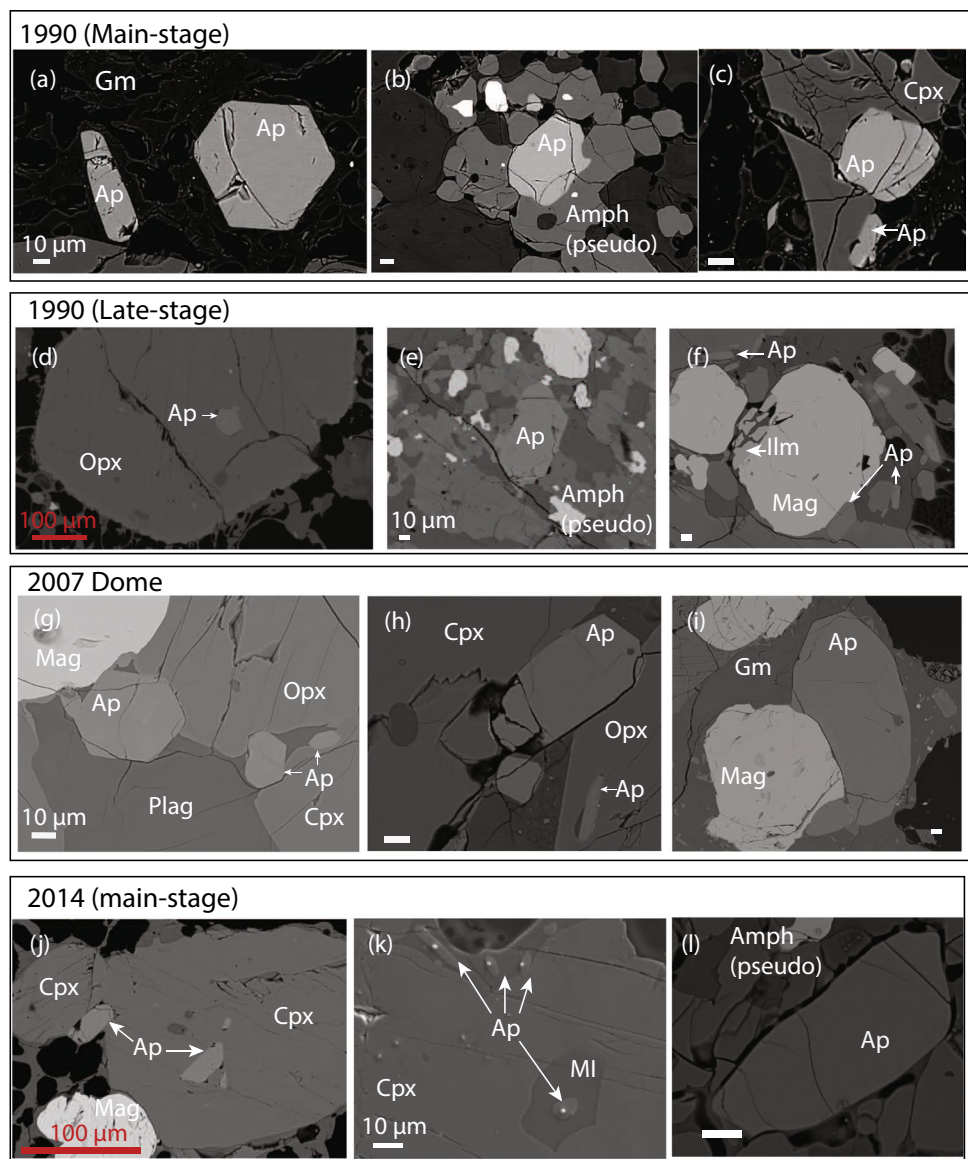
crystals of the 2007 dome rocks. We found timescales of up to 175 days were found, although 65% of them are ≤ 60 days (See Table 1 and Fig. 5). Most of the zoned apatite crystals from the 2007 eruption were in contact with the melt. Moreover, one apatite crystal was included in an amphibole pseudomorph (timescale of around 1 day), which may record time since amphibole breakdown, and the apatite's exposure to the melt. We believe that such a short timescale reflects the apatite crystal's limited exposure to the melt with different volatile contents before they were partially to fully enclosed as inclusions in other minerals, compared to those fully exposed in the melt These observations supports our assumption of an initial homogeneous composition, and the hypothesis that the zoning

we observe in apatite is related to ascent and associated changes in the melt.

We also found that apatite compositional profiles closer to the crystallographic *a*-axis systematically record timescales that are at least 2.5 times longer (63–175 days) than those closer to the *c*-axis (1–58 days). This difference is most noticeable where multiple profiles were measured on the same crystal. Such discrepancy could stem from a paucity in the knowledge and limited data on diffusion coefficients of volatile elements along the *a*-axis. We further observe no systematic difference between the times obtained from crystals that are mainly reversely zoned in Cl vs. those that are mainly zoned in F. Due to the potential kinetic delays between magma degassing, microlite crystallization and reaction of

Fig. 2 Ternary plots of volatile compositions (in mol %) of point analysis and profiles of apatite and elemental maps from the 2007 dome. Note that the crystals show significant chemical zoning. Ternary plot of volatile compositions (in mol. %) of 2007 apatite point analyses, with white symbols are the 2007 apatite and black symbols are apatite from other eruptions. (b) Ternary plot showing cores and rims compositions of apatite profiles, where rims are relatively more enriched in Cl compared to cores. Elemental maps show spatial variations in Cl and F concentrations: (c) apatite wedged between two phenocrysts; (d) Cpx-hosted apatite, and (e) groundmass apatite
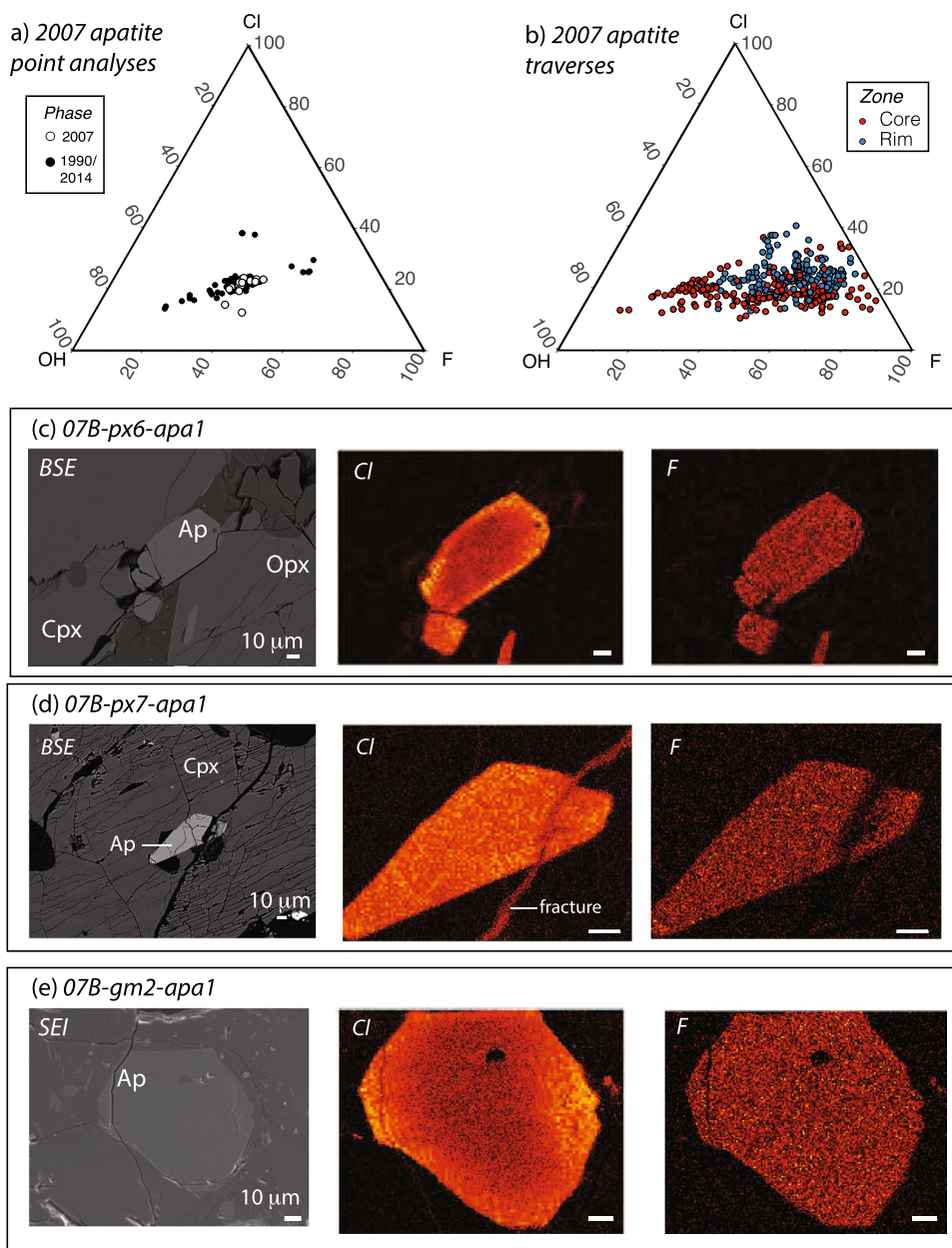
the apatite's F-Cl-OH concentrations to these processes, the calculated times are likely to be the minima especially for crystals that are not directly in contact with the external melt.

In relating the apatite timescales with the pre-eruptive unrest signals observed before the 2007 eruption, we interpret the cluster of timescales < 30 days as the final stage of magma ascent that began in early October and continued until the eruption date (see Supplementary Material Figs. S1, S2, S3). These dates overlap with the onset of different types of unrest in October 2007, such as seismic swarms, increases in seismic energy released, and inflation/deflation (Hidayati et al. 2019) (Fig. S1, S2). The relationships between the timing from the apatite zoning and the monitoring data thus indicate magma movement and ascent towards the surface prior to the dome emplacement (Fig. S3). Moreover, timescales > 60 days belong to profiles that were measured along the *a*-axis. Given the limited experimental constraints on the diffusion coefficients along this crystallographic axis, we are cautious about directly correlating these timescales with any unrest signal and ascribing them to magma ascent.

For the 2007 dome, we considered the possibility that volatile diffusion in apatite could continue after/during the lava dome emplacement, as it cooled much more slowly that the explosive eruptions. For this we calculated closure temperature of Cl in apatite, as described in Costa (2021). For a 50 μm crystal and a range of cooling rates (0.001–1 °C/

Fig. 3 Ternary plots of volatile compositions (in mol %) of point analysis and profiles of apatite and elemental maps from the 1990 and 2014 eruptions. Note that the crystals show limited to no chemical zoning of these elements. (a) Ternary plot of volatile compositions (in mol. %) of 1990 apatite point analyses, with white symbols are the 1990 apatite and black symbols are apatite from other eruptions. Circles are main-stage apatite, and squares are late-stage apatite. (b) Ternary plot of volatile compositions (in mol. %) of 2014 apatite point analyses. Below this plot is ternary plot showing cores and rims compositions of apatite profiles. X-ray elemental maps show Cl and F distributions. (c) Cpx-hosted inclusions (2014); (d) Amph-hosted apatite (2014), and (e) groundmass apatite (1990)

(a) *1990 apatite point analyses*

(b) *2014 apatite analyses (points + traverse)*

(c) 2014 clinopyroxene-hosted apatite, 14PUMI2-2-px3-apa1

(d) 2014 amphibole-hosted apatite, 14PUMI1-amph-apa6

(e) 1990 main-stage groundmass apatite, PL1new-px4-apa1
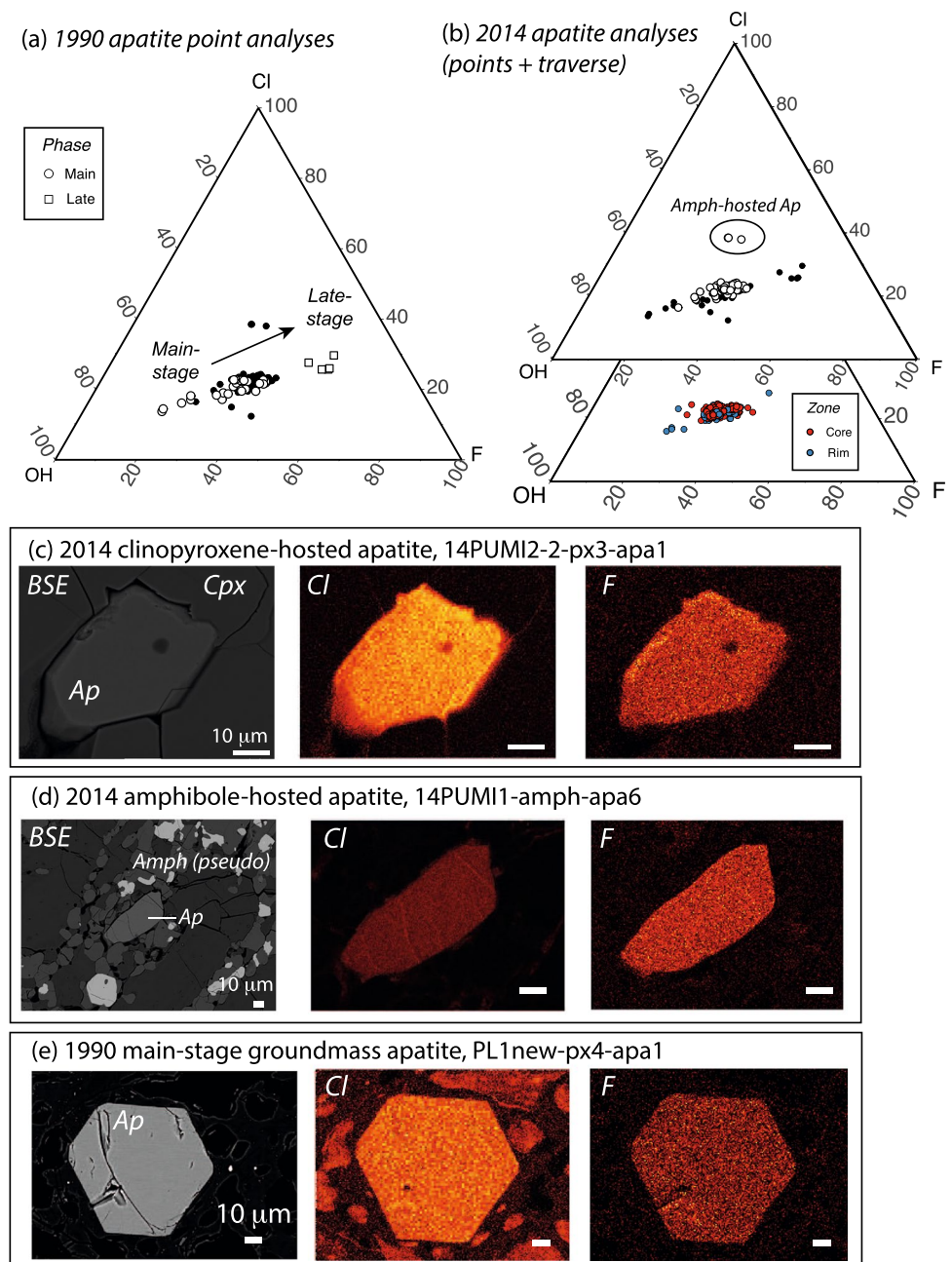
year), we found the closure temperature varies from 554 to 704 °C. This suggests that in principle, Cl re-equilibration could have continued during dome cooling. However, these temperatures are lower than that of a nearly dry solidus of the system, meaning at that point there would be no melt left that the apatite could re-equilibrate and exchange with. Thus we believe that there should be limited or no effect of dome cooling on the retrieved time scales.

The 1990 and 2014 eruptions.

The apatite crystals from the 1990 and 2014 deposits (we observed six in total) are unzoned in Cl, F, and OH at the scale of the EPMA maps and profiles. This lack of zoning likely reflects fast magma ascent, and thus limited transport time to be able to develop measurable chemical zoning. Notwithstanding, we can only calculate the time that would be required to generate an observable zoning length with the analytical techniques we have used. We found that using a length of 4 μm (i.e. the spatial resolution of our measurements) implies a maximum time of diffusion of 7–8 h, which means that the magmas would have been transported from their reservoir to the surface in less than this time. These maximum time-scales are shorter than the 1990 and 2014 total unrest (1–3 months—Lesage and Surono 1995; Hidayati et al.

Fig. 4 Two representative examples of compositional profiles of apatite crystals for the 2007 dome, with diffusion timescales calculated using ApTimer (Matlab version) from Li et al. (2020). Blue dashed line of each profile is the initial profile before diffusion. Red solid line shows the diffused model profile. In type 1 zoning, X_{Cl} increases from core to rim: (a) SEI image of groundmass apatite, with red arrow showing the profile. Inset shows a pole figure with the c-axis and a-axes. Orientation of the start of the profile is given as 'trv'. (b) X_{Cl} profile from rim to core. (c) X_F profile from rim to core. (d) X_{OH} profile from rim to core, which is a mirror image of X_F. In type 2 zoning, X_F increases from core to rim: (e) BSE image of apatite embedded in phenocrysts, with red arrow showing the profile. Inset shows pole figure with similar information as in (a). (f) X_{Cl} profile from rim to core. (g) X_F profile from rim to core. (h) X_{OH} profile from rim to core, which increases as in X_F

Contrasting magma ascent rates for explosive and dome eruptions
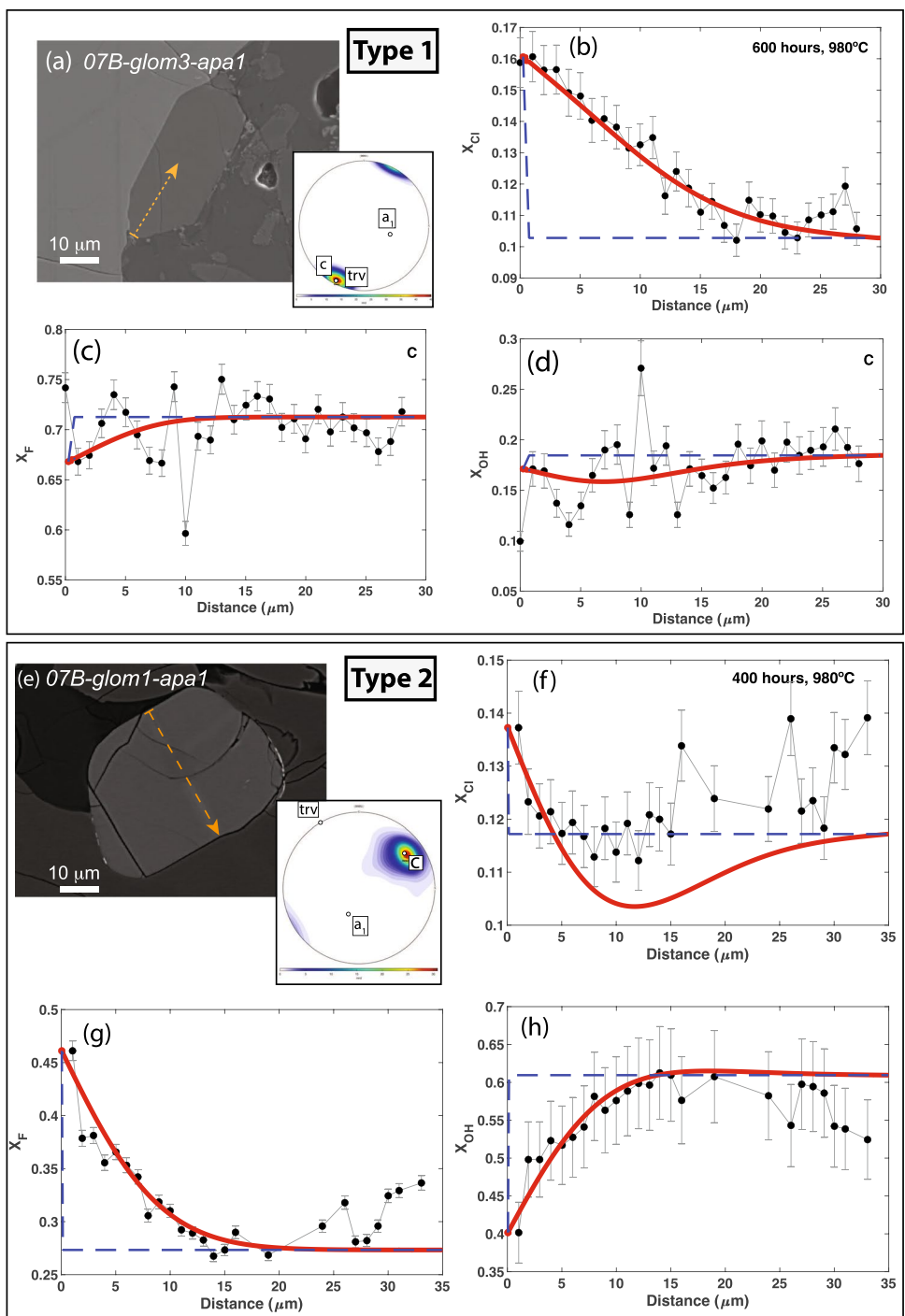
2019; Utami et al. 2021) but are of the same order of magnitude as the increase in seismic unrest directly before the eruptions (12–48 h; Lesage and Surono 1995; Hidayati et al. 2019). The relationship between the maximum timescales and the duration of unrest suggests that for the 1990 and 2014 eruptions, degassing and magma ascent occurred within 12–48 h before eruption. Such short timescales of ascent likely account for the fast escalation of seismicity before eruption.

We can estimate the magma ascent rates of Kelud by combining the timescales from apatite and the magma storage pressure estimated from phase equilibria experiments, mineral geobarometers, and volatile saturation pressures (Utami et al. 2021, 2022). The pressure was converted into depths below the edifice using an averaged density of the
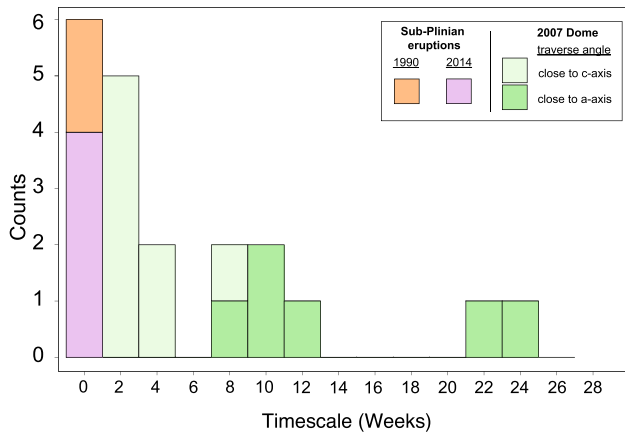
Fig. 5 Histogram of timescales of zoned crystals from the 2007 dome of Kelud. The timescales are divided into two groups: timescales where the acute angles of the profile is closer to the c-axis (light green), and timescales where the acute angles of the profile is closer to the a-axis (dark green)

crust of 2640 kg m^{-3}, which was previously proposed for the upper crust under Kelud (Jeffery et al. 2013). Utami et al. (2021; 2022) reported a range of storage pressures from 160 to > 400 MPa depending on the minerals, which suggests a melt and mineral distribution across a range of depths underneath Kelud, with most crystals around 100–200 MPa. Here we chose an intermediate pressure of 175 MPa (average of 150–200 MPa) according to phase equilibria experiments (Utami et al. 2022), that best matches the phase assemblage and phenocryst content of the three magmas and corresponds to a depth of ~ 6–7 km below the crater.

We find that the calculated ascent rates for the 2007 dome in this manner vary between 0.4–78 × 10^{-3} m s^{-1} but most are between 2.6–39 × 10^{-3} m s^{-1} for the 2007 dome (Table 1). These ascent rates from the apatite crystals are comparable or faster than the extrusive rates from other dome building eruptions such as Mt St Helens and Soufriere Hills (1–8 × 10^{-3} m s^{-1}) (Devine et al. 1998). Our calculated ascent rates are only estimates of their mean values, as magma ascent rate changes depending on processes occurring as the magma moves towards the surface, and the magma storage depth is for the 2007 is less well defined than for the 1990 and 2014 eruptions (Utami et al. 2022). Moreover, Utami et al. (2022) has shown that the 2007 magma re-equilibrated as it moved towards the surface to lower melt water contents of around 1 wt. %. In such a scenario, we calculated a saturation pressure of about 77 MPa with MagmaSat (Ghiorso and Gualda 2015) using the calculated matrix composition given in Utami et al. (2022), along with 336 ppm CO_2 from Cassidy et al. (2019). This corresponds to about 77 MPa and 3 km depth, which would imply even slower ascent rates. For an apatite crystal that recorded a timescale of 25 days, the reduction in depth to

77 MPa would result in a threefold reduction in the ascent rate from 3 × 10^{-3} m s^{-1} to 1 × 10^{-3} m s^{-1}. With our longest diffusion timescale of 175 days, we would even reduce the ascent rate to 2 × 10^{-4} m s^{-1}.

For the 1990 and 2014 magmas we only obtained minimum magma ascent rates of about 3.0 × 10^{-1} m s^{-1} from our estimated maximum transfer times, as discussed in the previous section. These are more than an order of magnitude higher than those of the 2007 dome magma. Such a difference in ascent rates would account for the contrasting eruption styles, where the magmas feeding explosive eruptions would be able to retain their dissolved volatile content, but the slow ascent would allow the dome to release the volatiles through permeable degassing (Gonnermann and Manga 2013). These ascent rates are significantly lower than the rates of 4–5 m s^{-1} previously proposed for the 2014 eruption of Kelud (Cassidy et al. 2019), but we note that the difference in ascent
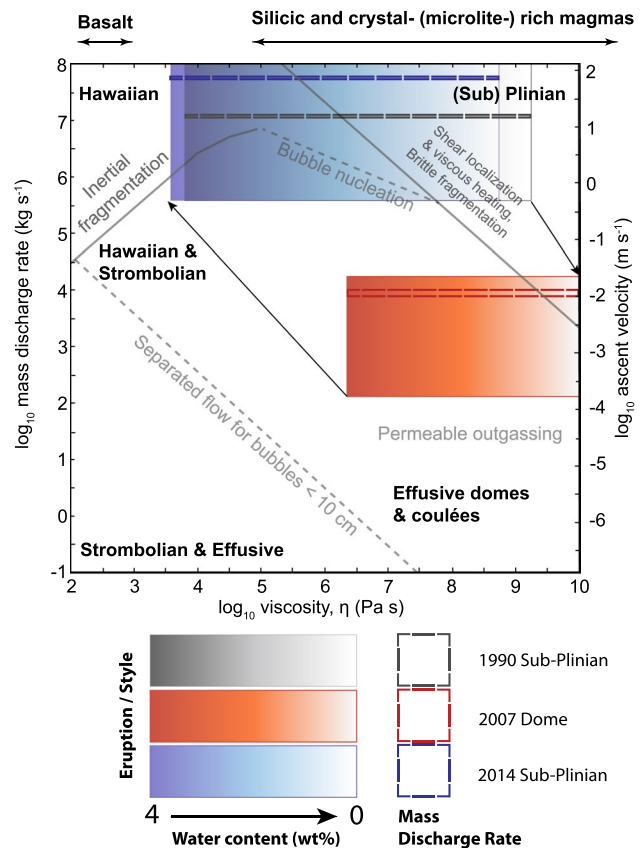

Fig. 6 Viscosity vs. ascent rate and mass discharge rate, modified after Fig. 4.10 of Gonnermann and Manga (2013). The magma ascent rates were derived from apatite diffusion modelling and viscosity calculated for Kelud magmas in Table 3. Coloured boxes represent the region outlined by magma viscosity vs. ascent velocity observed for the 1990 (grey), 2007 (red), and 2014 (blue) eruptions for a range of dissolved water content in the melt. Boxes with dashed lines are the average to maximum mass discharge rates determined by Maeno et al. (2019)

rates also depends on the chosen pre-eruptive magma storage depths (~ 7 km used in our study from Utami et al. (2021, 2022) vs 2–3 km in Cassidy et al. (2019)). Nonetheless, our estimates are still comparable with the range of ascent rates for explosive eruptions from volcanoes including Mt St Helens and Soufrière Hills (Rutherford 2008). We find that ascent rates for explosive eruptions of Kelud overlaps with rates from other historical eruptions from basaltic andesite volcanoes, such as 1974 eruption of Volcan de Fuego, and the 1986 eruption of Izu-Oshima (Cassidy et al. 2018).

Relating ascent rates to eruptive styles

Many volcanoes show a range of eruptive styles, and these are likely controlled by magmatic processes resulting in rapid changes in pre-eruptive and syn-eruptive parameters (e.g. Cassidy et al. 2018; Annen and Burgisser 2021; Annen et al. 2023). Ultimately, magma fragmentation is involved in the explosivity of a given eruption (Dingwell et al. 1993), a process that is highly dependent on the physical properties of the magma and fluids, including the effective viscosity. We hereby attempt to relate the ascent rates to the effective viscosities to investigate the dominant processes controlling explosive and effusive eruptions at Kelud volcano, as proposed by Gonnermann and Manga (2013).

The magma viscosities of 1990 and 2014 explosive events are quite different from the 2007 dome, mainly because of the much higher phenocryst content of the latter (Table 3; Fig. 6). The magma viscosity models of Faroughi and Huber (2015), Costa et al. (2009), and Caricchi et al. (2007) yield comparable effective viscosity ranges for the 1990 ($10^{3.8}$ -$10^{7.7}$ Pa s) and 2014 ($10^{3.6}$–$10^{7.2}$ Pa s) eruptions for a minimum magma ascent rate of $> 3 \times 10^{-1}$ m s^{-1}, respectively. These magma viscosities are also somewhat comparable to estimates from the viscosity model of Moitra and Gonnermann (2015, Moitra et al. 2018) for the 1990 ($10^{5.8}$–$10^{9.3}$ Pa s) and 2014 ($10^{4.5}$–$10^{8.7}$ Pa s), which give slightly higher estimates compared to the previous models, but still overlap with those calculated using the Einstein-Roscoe equation for the same eruptions (1990 = $> 10^{4.2}$–$10^{7.8}$ Pa s; 2014 = $> 10^{4.0}$–$10^{7.5}$ Pa s). In contrast, the 2007 dome span a wide range of effective viscosities for the given magma ascent rate (10^{-4} to 10^{-2} m s^{-1}). The magma viscosity models of Faroughi and Huber (2015), Costa et al. (2009), and Caricchi et al. (2007) yield effective viscosities for the 2007 dome of $10^{8.0}$–$10^{13.3}$ Pa s. The viscosity for the 2007 dome ($10^{6.4}$ -$10^{11.0}$ Pa s) using the model of Moitra and Gonnermann (2015, Moitra et al. 2018) give slightly lower effective viscosities relative to other models. Despite these range of viscosities between the different models, most of the models either give consistent ranges (Faroughi and Huber 2015; Costa et al. 2009; and Caricchi et al. 2007), or overlap with the other models as in the case of Moitra and Gonnermann (2015, Moitra et al. 2018). Hence we shall consider all models in our interpretation (See Table 3 and Fig. 6).

We used the relationship proposed in Gonnermann and Manga (2013) to connect the magma viscosity and magma ascent rates to eruptive styles (Fig. 6). We find that the initial processes dominating the 1990 and 2014 explosive eruptions are inertial fragmentation and bubble nucleation, straddling the Hawaiian and sub-Plinian fields. In the 1990 and 2014 sub-Plinian eruptions (e.g. Maeno et al. 2019), we propose that syn-eruptive processes such as degassing and microlite crystallization would promote an increasingly viscous magma that rapidly rose to the surface with buoyancy driven ascent due to fluid accumulation. The magma would then eventually evolve towards sub-Plinian field (assuming to proceed from left to right on Fig. 6), where shear localization, viscous heating, and brittle fragmentation dominate (Gonnermann and Manga 2013). These processes contrast with the dominant process for the 2007 dome, which is primarily permeable outgassing. The data shows some overlap with the sub-Plinian field, but the combination of slow ascent and outgassing would make the 2007 magma so degassed that processes such as brittle fragmentation were unlikely to happen.

The ascent rates we calculated for the 1990 and 2014 events imply mass discharge rates $> 10^{5.5}$ kg s^{-1}, which overlaps with discharge rates (10^7–10^8 kg s^{-1}) independently determined for the same eruptions by Maeno et al. (2019). Combining the magma viscosity with the discharge rate for the 2007 dome (5.8×10^3—1.9×10^4 kg s^{-1}) (Maeno et al. 2019), we find that the corresponding velocity becomes slightly higher at around $10^{-1.5}$ m s^{-1}. This velocity overlaps with the upper range of the ascent rates determined from apatite, but as the MDR is estimated at the vent exit conditions, the corresponding exit velocities of the 1990 and 2014 eruptions are expected to be significantly higher than the one we estimated with apatite. Moreover, these relationships do not typically consider the presence of an exsolved volatile phase at pre-eruptive conditions as we have proposed for the 1990 and 2014 eruptions (Utami et al. 2022), and which should have an influence on the viscosity, magma ascent rates, and eruptive style relations (Cassidy et al. 2018). Notwithstanding these limitations, we find it remarkable that magma ascent rates derived from apatite are consistent with other parameters such as discharge rates, which potentially enables us to characterize different eruption styles.

Conclusions

The duration and rates of magma ascent are considered to be key parameters that control the eruption style. Here we show that using the volatile zoning (F-Cl-OH) in apatite from the last three eruptions of Kelud volcano (1990, 2007, 2014), it

is possible to gain insights into explosive and effusive eruptions at Kelud volcano, Indonesia using apatite. Unzoned apatite from the explosive eruptions of 1990 and 2014 record evidence for minimum ascent rates of $> 3.0 \times 10^{-1}$ m s^{-1}. In contrast, reversely zoned apatite from the 2007 dome rocks record evidence for considerably slower ascent rates ($> 0.4 \times 10^{-3}$ m s^{-1}). The estimated ascent rates for the 1990 explosive eruptions overlap with magma ascent rates constrained through the onset of exponential increase in seismicity directly prior to the eruption as previously observed in Lesage and Surono (1995). Our ascent rates are consistent with ascent rates from other volcanoes with effusive and explosive eruptions (e.g. Mount St Helens, Soufriere Hills, Unzen) (Rutherford 2008), and thus we can establish a lower bound on the ascent rates of explosive eruptions for Kelud and other analogous volcanoes. The reversely zoned apatite from the 2007 dome allows us to estimate timescales of buoyancy driven magma ascent towards dome emplacement, which overlaps with the seismic and geodetic unrest (Lesage and Surono, 1995; Lubis 2014). Magma viscosity and ascent relationships show that whereas the 1990 and 2014 eruptions are typical sub-Plinian eruptions with dominating processes including brittle fragmentation, bubble nucleation, and shear localization, dome emplacement is likely dominated by permeable outgassing. Our study demonstrates the utility of apatite to shed light on variations in eruption style for volatile dominant processes at active volcanoes such as Kelud to record timescales of ascent and rates that are consistent with eruptive style at active volcanoes.

Supplementary Information The online version contains supplementary material available at https://doi.org/10.1007/s00445-023-01698-1.

Author Contributions **SBU:** Conceptualization, investigation, project administration, methodology, fieldwork and sampling, formal analyses, data curation, visualization, writing (original draft; review and editing). **FC:** Supervision, conceptualization, investigation, resources, methodology, writing – review & editing, supervision, project administration, funding acquisition, final approval of manuscript. **HH:** fieldwork and sampling, supervision.

References

Albert H, Costa F, Marti J (2015) Timing of magmatic processes and unrest associated with mafic historical monogenetic eruptions in tenerife island. J Petrol 56(10):1945–1966

Andújar J, Costa F, Scaillet B (2013) Storage conditions and eruptive dynamics of central versus flank eruptions in volcanic islands: The case of tenerife (Canary Islands, Spain). J Volcanol Geoth Res 260:62–79. https://doi.org/10.1016/j.jvolgeores.2013.05.004

Annen C, Burgisser A (2021) Modeling Water Exsolution from a Growing and Solidifying Felsic Magma Body. Lithos 402:105799–105799. https://doi.org/10.1016/j.lithos.2020.105799

Annen C, Pinel V, Burgisser A (2023) Re-evaluation of the role of volatiles in the rupture of magma chambers and the triggering of crystal-rich eruptions. J Volcanol Geoth Res 435. https://doi.org/10.1016/j.jvolgeores.2023.107755

Bernard O, Bouvet de Maisonneuve C (2020) Controls on Eruption Style at Rabaul, Papua New Guinea – Insights from Microlites, Porosity and Permeability Measurements. J Volcanol Geoth Res 406:107068. https://doi.org/10.1016/j.jvolgeores.2020.107068

Bernard O, Li W, Costa F, Saunders S, Itikarai I, Sindang M, Bouvet de Maisonneuve C (2022) Explosive-effusive-explosive: The role of magma ascent rates and paths in modulating caldera eruptions. Geology 50(9):1013–1017

Blake DM, Wilson G, Stewart C, Craig HM, Hayes J, Jenkins S, Wilson T, Horwell CJ, Andreastuti S, Daniswara R, Ferdiwijaya D, Leonard GS, Hendrasto M, Cronin S (2015) The 2014 eruption of Kelud volcano. Indonesia : impacts on infrastructure, utilities, agriculture and health. 15:1–131

Blundy J, Cashman K (2000) Degassing and crystallization of ascending andesite and Dacite. Philos Trans Royal Soc A: Math, Phys Eng Sci 358(1770):1487–1513

Blundy J, Cashman K (2008) Petrologic reconstruction of magmatic system variables and processes. Rev Mineral Geochem 69(1):179–239

Boyce JW, Tomlinson SM, McCubbin FM, Greenwood JP, Treiman AH (2014) The lunar apatite paradox. Science 344(6182):400–402. https://doi.org/10.1126/science.1250398

Bull KF, Buurman H (2013) An overview of the 2009 eruption of redoubt volcano, Alaska. J Volcanol Geotherm Res 259:2–15. https://doi.org/10.1016/j.jvolgeores.2012.06.024

Cadoux A, Scaillet B, Druitt TH, Deloule E (2014) Magma storage conditions of large Plinian eruptions of Santorini volcano (Greece). J Petrol 55(6):1129–1171. https://doi.org/10.1093/petrology/egu021

Caricchi L, Burlini L, Ulmer P, Gerya T, Vassalli M, Papale P (2007) Non-newtonian rheology of crystal-bearing magmas and implications for magma ascent dynamics. Earth Planet Sci Lett 264(3–4):402–419. https://doi.org/10.1016/j.epsl.2007.09.032

Cassidy M, Manga M, Cashman K, Bachmann O (2018) Controls on explosive-effusive volcanic eruption styles. Nat Commun 9(1):2839. https://doi.org/10.1038/s41467-018-05293-3

Cassidy M, Ebmeier SK, Helo C, Watt SFL, Caudron C, Odell A, Spaans K, Kristianto P, Triastuty H, Gunawan H, Castro JM (2019) Explosive eruptions with little warning: experimental petrology and volcano monitoring observations from the 2014 eruption of Kelud, Indonesia. Geochem Geophys Geosystems 20:4218–4247. https://doi.org/10.1029/2018GC008161

Caudron C, Mazot A, Bernard A (2012) Carbon dioxide dynamics in Kelud volcanic lake. J Geophys Res 117:B05102. https://doi.org/10.1029/2011JB008806

Costa F (2021) Clocks in magmatic rocks. Annu Rev Earth Planet Sci 49:231–252

Costa F, Dohmen R, Chakraborty S (2008) Time scales of magmatic processes from modeling the zoning patterns of crystals. Rev Mineral Geochem 69(1):545–594

Costa A, Caricchi L, Bagdassarov N (2009) A model for the rheology of particle-bearing suspensions and partially molten rocks. Geochem Geophys Geosyst 10(3):1–13. https://doi.org/10.1029/2008GC002138

Costa F, Andreastuti S, Bouvet de Maisonneuve C, Pallister JS (2013) Petrological insights into the storage conditions, and magmatic processes that yielded the centennial 2010 Merapi explosive eruption. J Volcanol Geoth Res 261:209–235

Couch S, Sparks RSJ, Carroll MR (2003) The Kinetics of Degassing-Induced Crystallization at Soufriere Hills Volcano, Montserrat. J Petrol 44(8):1477–1502. https://doi.org/10.1093/petrology/44.8.1477

Devine JD, Rutherford MJ, Gardner JE (1998) Petrologic Determination of Ascent Rates for the 1995–1997 Soufriere Hills Volcano Andesitic Magma. Geophys Res Lett 25(19):3673–3676. https://doi.org/10.1029/98GL00912

Dingwell DB (1996) Volcanic Dilemma-Flow or Blow? Science 273(5278):1054–1055. https://doi.org/10.1126/science.273.5278.1054

Dingwell DB, Bagdasarov NS, Bussod GY, Webb SL (1993) Magma Rheology. In: Luth RW (ed) Experiments at high pressure and applications to the earth's mantle: short course handbook, 21. Mineralogical Association of Canada, Edmonton, pp 131–196

Dohmen R, Chakraborty S (2002) Si and O Diffusion in Olivine and Implications for Characterizing Plastic Flow in the Mantle. Geophys Res Lett 29(21):2030. https://doi.org/10.1029/2002GL015480

Einstein A (1906) Effect of suspended rigid spheres on viscosity. Ann Phys 19:289–306

Faroughi SA, Huber C (2015) A generalized equation for rheology of emulsions and suspensions of deformable particles subjected to simple shear at low reynolds number. Rheol Acta 54(2):85–108. https://doi.org/10.1007/s00397-014-0825-8

Georgeais G, Koga KT, Moussallam Y, Rose-Koga EF (2021) Magma decompression rate calculations with EMBER: a user-friendly software to model diffusion of H2O, CO2, and S in melt embayments. Geochem Geophys Geosystems 22:e2020GC009542. https://doi.org/10.1029/2020GC009542

Ghiorso MS, Gualda GA (2015) An H 2 O-CO 2 mixed fluid saturation model compatible with rhyolite-MELTS. Contrib Miner Petrol 169:1–30

Giordano D, Russell JK, Dingwell DB (2008) Viscosity of Magmatic Liquids: A Model. Earth Planet Sci Lett 271(1):123–134

Global Volcanism Program (1991) Report on Kelud (Indonesia). In: McClelland L (ed) Bulletin of the global volcanism network, vol 16. Smithsonian Institution, p 3. https://doi.org/10.5479/si.GVP.BGVN199103-263280

Global Volcanism Program (1996) Report on Kelud (Indonesia). In: Wunderman R (ed) Bulletin of the global volcanism network, vol 21. Smithsonian Institution, p 11. https://doi.org/10.5479/si.GVP.BGVN199611-263280

Global Volcanism Program (2001) Report on Kelud (Indonesia). In: Wunderman R (ed) Bulletin of the global volcanism network, vol 26. Smithsonian Institution, p 2. https://doi.org/10.5479/si.GVP.BGVN200102-263280

Global Volcanism Program, 2013. Kelud (263280) in [Database] Volcanoes of the World (v. 4.11.2; 02 Sep 2022). Distributed by Smithsonian Institution, compiled by Venzke, E. https://doi.org/10.5479/si.GVP.VOTW4-2013

Gonnermann HM, Manga M (2013) Dynamics of magma ascent in the volcanic conduit. In: Fagents S, Gregg TKP, Lopes RMC (eds) Modeling volcanic processes: The physics and mathematics of volcanism. Cambridge University Press, pp 55–84. https://doi.org/10.1017/CBO9781139021562.004

Goode LR, Handley HK, Cronin SJ, Abdurrachman M (2018) Insights into Eruption Dynamics from the 2014 Pyroclastic Deposits of Kelut Volcano, Java, Indonesia, and Implications for Future Hazards. J Volcanol Geoth Res. https://doi.org/10.1016/J.JVOLGEORES.2018.02.005

Harlow DE (2015) Apatite: A Fingerprint for Metasomatic Processes. Elements 11(3):171–176. https://doi.org/10.2113/gselements.11.3.171

Hidayati S, Basuki A, Kristianto K, Mulyana I (2009) Emergence of lava dome from the crater lake of Kelud Volcano East Java. Indones J Geosci 4(4):229–238

Hidayati S, Triastuty H, Mulyana I, Adi S, Ishihara K, Basuki A, Kuswandarto H, Priyanto B, Solikhin A (2019) Differences in the seismicity preceding the 2007 and 2014 Eruptions of Kelud Volcano, Indonesia. J Volcanol Geoth Res 382:50–67. https://doi.org/10.1016/j.jvolgeores.2018.10.017

Humaida H (2013) A geochemical study on Merapi and Kelud volcanic eruptions [Doctoral dissertation]. Universitas Gadjah Mada

Humphreys MCS, Smith VC, Coumans JP, Riker JM, Stock MJ, de Hoog JCM, Brooker RA (2021) Rapid pre-eruptive mush reorganisation and atmospheric volatile emissions from the 12.9 ka laacher see eruption, determined using apatite. Earth Planet Sci Lett 576:117198–117198. https://doi.org/10.1016/j.epsl.2021.117198

Jeffery AJ, Gertisser R, Troll VR, Jolis EM, Dahren B, Harris C, Tindle AG et al (2013) The Pre-eruptive magma plumbing system of the 2007–2008 dome-forming eruption of Kelut Volcano, East Java, Indonesia. Contrib Miner Petrol 166(1):275–308

Ketcham RA (2015) Technical note: Calculation of Stoichiometry from EMP Data for Apatite and other phases with mixing on monovalent anion sites. Am Miner 100(7):1620–1623. https://doi.org/10.2138/am-2015-5171

Kilgour GN, Saunders KE, Blundy JD, Cashman KV, Scott BJ, Miller CA (2014) Timescales of magmatic processes at Ruapehu volcano from DIFFUSION chronometry and their comparison to monitoring data. J Volcanol Geoth Res 288:62–75

Kusumadinata K, Indonesia Direktorat Vulkanologi (1979) Data dasar gunungapi indonesia = catalogue of references on indonesian volcanoes with eruptions in historical time. Indonesia: Republik Indonesia Departemen Pertambangan dan Energi Direktorat Jenderal Pertambangan Umum Direktorat Vulkanologi

Lesage PS (1995) Seismic Precursors of the February 10, 1990 Eruption of Kelut Volcano, Java. J Volcanol Geoth Res 65(1):135–146

Li W, Costa F (2019) A thermodynamic model for F-Cl-OH partitioning between silicate melts and apatite including non-ideal mixing with application to constraining melt volatile budgets. Geochim Cosmochim Acta 269:203–222. https://doi.org/10.1016/j.gca.2019.10.035

Li W, Chakraborty S, Nagashima K, Costa F (2020) Multicomponent diffusion of F, Cl and OH in apatite with application to magma ascent rates. Earth Planet Sci Lett 550:116545–116545. https://doi.org/10.1016/j.epsl.2020.116545

Li W, Costa F, Nagashima K (2021) Apatite Crystals reveal melt volatile budgets and magma storage depths at Merapi volcano, Indonesia. J Petrol 62(4). https://doi.org/10.1093/petrology/egaa100

Lubis AM (2014) Uplift of Kelud volcano prior to the November 2007 eruption as Observed by L-Band Insar. J Eng Technol Sci 46(3):245–257

Maeno F, Nakada S, Yoshimoto M, Shimano T, Hokanishi N, Zaennudin A, Iguchi M (2019) Eruption Pattern and a Long-Term Magma Discharge Rate over the Past 100 Years at Kelud Volcano Indonesia. J Disaster Res 14(1):27–39. https://doi.org/10.20965/JDR.2019.P0027

Martel C (2012) Eruption dynamics inferred from microlite crystallization experiments: Application to Plinian and Dome-Forming eruptions of Mt. Pelée (Martinique, Lesser Antilles). J Petrol 53(4):699–725. https://doi.org/10.1093/petrology/egr076

Martel C, Schmidt BC (2003) Decompression experiments as an insight into ascent rates of silicic magmas. Contrib Miner Petrol 144(4):397–415. https://doi.org/10.1007/s00410-002-0404-3

Moitra P, Gonnermann HM (2015) Effects of crystal shape- and size-modality on magma rheology. Geochem Geophys Geosyst 16:1–26. https://doi.org/10.1002/2014GC005554

Moitra P, Gonnermann HM, Houghton BG, Tiwary CS (2018) Fragmentation and plinian eruption of crystallizing basaltic magma. Earth Planet Sci Lett 500:97–104. https://doi.org/10.1016/j.epsl.2018.08.003

Myers ML, Wallace PJ, Wilson CJN (2019) Inferring magma ascent timescales and reconstructing conduit processes in explosive rhyolitic eruptions using diffusive losses of hydrogen from melt Inclusions. J Volcanol Geoth Res 369:95–112. https://doi.org/10.1016/j.jvolgeores.2018.11.009

Myers ML, Druitt TH, Schiavi F, Gurioli L, Flaherty T (2021) Evolution of magma decompression and discharge during a Plinian event (late bronze-age eruption, Santorini) from multiple eruption-intensity proxies. Bull Volcanol 83(18). https://doi.org/10.1007/s00445-021-01438-3

Nakamichi H, Iguchi M, Triastuty H, Hendrasto M, Mulyana I (2017) Differences of precursory seismic energy release for the 2007 effusive dome-forming and 2014 Plinian eruptions at Kelud Volcano, Indonesia. J Volcanol Geoth Res 382:68–80. https://doi.org/10.1016/j.jvolgeores.2017.08.004

Nathwani CL, Loader MA, Wilkinson JJ, Buret Y, Sievwright RH, Hollings P (2020) Multi-stage arc magma evolution recorded by apatite In volcanic rocks. Geology 48(4):323–327. https://doi.org/10.1130/G46998.1

Padang MN (1983) History of the volcanology in the former Netherlands East Indies. Scripta Geol 71:1–76

Passarelli L, Brodsky EE (2012) The Correlation between run-up and repose times of volcanic eruptions. Geophys J Int 188(3):1025–1045. https://doi.org/10.1111/j.1365-246X.2011.05298.x

Preece K, Gertisser R, Barclay J, Berlo K, Herd RA, Facility EIM (2014) Pre- and syn-eruptive degassing and crystallisation Processes of the 2010 and 2006 Eruptions of Merapi Volcano, Indonesia. Contrib Miner Petrol 168(4):1–25. https://doi.org/10.1007/s00410-014-1061-z

Puspito NT, Shimazaki K (1995) Mantle structure and seismotectonics of the Sunda and Banda Arcs. Tectonophysics 251(1–4):215–228. https://doi.org/10.1016/0040-1951(95)00063-1

Putirka KD (2008) Thermometers and barometers for volcanic systems. Rev Mineral Geochem 69(1):61–120

Rasmussen DJ, Plank TA, Roman DC, Power JA, Bodnar RJ, Hauri EH (2018) When does eruption run-up begin? multidisciplinary insight from the 1999 eruption of Shishaldin volcano. Earth Planet Sci Lett 486:1–14. https://doi.org/10.1016/j.epsl.2018.01.001

Roman DC, Cashman KV (2018) Top–down precursory volcanic seismicity: Implications for "Stealth" magma ascent and long-term eruption forecasting. Front Earth Sci 6:1–18. https://doi.org/10.3389/feart.2018.00124

Roscoe R (1952) The viscosity of suspensions of rigid spheres. Br J Appl Phys 3(8):267

Rutherford MJ (2003) Magmatic conditions and magma ascent as indicated by hornblende phase equilibria and reactions in the 1995–2002 soufriere hills magma. J Petrol 44(8):1433–1453. https://doi.org/10.1093/petrology/44.8.1433

Rutherford MJ (2008) Magma ascent rates. Rev Mineral Geochem 69:241–271. https://doi.org/10.2138/rmg.2008.69.7

Saalfeld MA, Myers ML, deGraffenried R, Shea T, Waelkens CM (2022) On the rise: using reentrants to extract magma ascent rates in the Bandelier Tuff caldera complex, New Mexico, USA. Bull Volcanol 84:1–21. https://doi.org/10.1007/s00445-021-01518-4

Saunders K, Blundy J, Dohmen R, Cashman K (2012) Linking petrology and seismology at an active volcano. Science 336(6084):1023–1027

Schneider CA, Rasband WS, Eliceiri KW (2012) NIH Image to ImageJ: 25 years of image analysis. Nat Methods 9(7):671–675. https://doi.org/10.1038/nmeth.2089

Scott JAJ, Humphreys MCS, Mather TA, Pyle DM, Stock MJ (2015) Insights into the Behaviour of S, F, and Cl at Santiaguito Volcano, Guatemala, from Apatite and Glass. Lithos 232:375–394. https://doi.org/10.1016/j.lithos.2015.07.004

Stock MJ, Humphreys MCS, Smith VC, Isaia R, Pyle DM (2016) Late-stage volatile saturation as a potential trigger for explosive volcanic eruptions. Nat Geosci 9(3):249–254. https://doi.org/10.1038/ngeo2639

Stock MJ, Humphreys MCS, Smith VC, Isaia R, Brooker RA, Pyle DM (2018) Tracking volatile behaviour in sub-volcanic plumbing systems using apatite and glass: Insights into pre-eruptive processes at Campi Flegrei, Italy. J Petrol 59(12):2463–2492. https://doi.org/10.1093/petrology/egy020

Toramaru A, Noguchi S, Oyoshihara S, Tsune A (2008) MND (Microlite Number Density) Water exsolution rate meter. J Volcanol Geoth Res 175(1–2):156–167. https://doi.org/10.1016/j.jvolgeores.2008.03.035

Utami SB, Costa F, Lesage P, Allard P, Humaida H (2021) Fluid fluxing and accumulation drive decadal and short-lived explosive basaltic andesite eruptions preceded by limited volcanic unrest. J Petrol 62(11). https://doi.org/10.1093/petrology/egab086

Utami SB, Andùjar J, Costa F, Scaillet B, Humaida H, Carn S (2022) Pre-eruptive excess volatiles and their relationship to effusive and explosive eruption styles in semi-plugged volcanoes. Front Earth Sci 10(September). https://doi.org/10.3389/feart.2022.882097

Vandemeulebrouck J, Sabroux J-C, Halbwachs M, Poussielgue N, Grangeon J, Tabbagh J et al (2000) Hydroacoustic noise precursors of the 1990 eruption of Kelut volcano, Indonesia. J Volcanol Geoth Res 97(1):443–456

Wang L-X, Marks MAW, Wenzel T, Von Der Handt A, Keller J, Teiber H, Markl G (2014) Apatites from the Kaiserstuhl volcanic complex, Germany: New constraints on the relationship between carbonatite and associated silicate rocks. Eur J Mineral 26(3):397–414. https://doi.org/10.1127/0935-1221/2014/0026-2377

Whelley PL, Newhall CG, Bradley KE (2015) The frequency of explosive volcanic eruptions in Southeast Asia. Bull Volcanol 77:1. https://doi.org/10.1007/s00445-014-0893208

Widiyantoro S, Ramdhan M, Métaxian JP, Cummins PR, Martel C, Erdmann S, Nugraha AD, Budi-Santoso A, Laurin A, Fahmi AA (2018) Seismic Imaging and petrology explain highly explosive eruptions of Merapi volcano, Indonesia. Sci Rep 8(1):1–7. https://doi.org/10.1038/s41598-018-31293-w

Widiyantoro S, van der Hilst R (1996) Structure and evolution of lithospheric slab beneath the Sunda arc. Indonesia. Science 271(5255):1566–1570

Williams GT, Jenkins SF, Biass S, Wibowo HE, Harijoko A (2020) Remotely assessing tephra fall building damage and Vulnerability: Kelud Volcano, Indonesia. J Appl Volcanol 9(1):1–18. https://doi.org/10.1186/s13617-020-00100-5